



# Electron beam induced deposition of rhodium from the precursor $[\text{RhCl}(\text{PF}_3)_2]_2$ : morphology, structure and chemical composition

F. Cicoira<sup>a,\*</sup>, K. Leifer<sup>b</sup>, P. Hoffmann<sup>a</sup>, I. Utke<sup>a</sup>, B. Dwir<sup>b</sup>, D. Laub<sup>c</sup>,  
P.A. Buffat<sup>c</sup>, E. Kapon<sup>b</sup>, P. Doppelt<sup>d</sup>

<sup>a</sup>Advanced Photonics Laboratory (APL), Swiss Federal Institute of Technology (EPFL), 1015 Lausanne, Switzerland

<sup>b</sup>Institute of Quantum Electronics and Photonics (IPEQ), Swiss Federal Institute of Technology (EPFL), 1015 Lausanne, Switzerland

<sup>c</sup>Central Facility of Electron Microscopy (CIME), Swiss Federal Institute of Technology (EPFL), 1015 Lausanne, Switzerland

<sup>d</sup>Ecole Supérieure de Physique et Chimie Industrielle-CNRS, 10 rue Vauquelin, 75231 Paris Cedex 05, France

Received 2 September 2003; accepted 9 February 2004

Communicated by D.T.J. Hurler

## Abstract

We have studied the morphology, the structure and the chemical composition of micro- and nano-structures grown by electron beam-induced deposition of  $[\text{RhCl}(\text{PF}_3)_2]_2$ . Transmission electron microscopy revealed that the deposits are made up of face centered cubic crystalline Rh grains (4–6 nm in diameter) immersed in an amorphous matrix. Auger electron spectroscopy and electron energy loss spectroscopy showed that a carbon contamination layer is present at the deposit surface, while the bulk material contains the elements Rh (60 at%), P (20 at%), Cl, O and N (remaining 20 at%). The structure, the chemical composition of the deposits and the size of the Rh nano-crystals are independent of the deposit shape and of the deposition parameters, within the range explored in this work.

© 2004 Elsevier B.V. All rights reserved.

PACS: 61.16.B; 81.15.J; 61.64

Keywords: A3. Chemical vapor deposition processes; B1. Nano-materials; A4. Electron energy loss spectroscopy; A5. Transmission electron microscopy

## 1. Introduction

Electron beam induced deposition (EBID) is a particularly attractive nano-fabrication technique. It allows high-density and high-resolution three-dimensional structuring in a single step. EBID is nowadays applied in small-scale fabrication of laboratory devices such as super-tips for scanning probe microscopy [1], photonic crystals [2],

\*Corresponding author. Istituto per lo Studio dei Materiali Nanostrutturati (ISMN), Consiglio Nazionale delle Ricerche (CNR), Via Gobetti 101, 40141 Bologna, Italy. Tel.: +39-0516398530; fax: +39-0516398540.

E-mail addresses: [f.cicoira@ism.bo.cnr.it](mailto:f.cicoira@ism.bo.cnr.it) (F. Cicoira), [patrik.hoffmann@epfl.ch](mailto:patrik.hoffmann@epfl.ch) (P. Hoffmann).

micro-field emitters [3], conducting lines [4], X-ray mask repair [5], and micro-opto-electronic devices [6]. The EBID growth process can be controlled by varying the electron beam parameters (current, energy, position, exposure time) and the precursor partial pressure, allowing a wide range of shapes. On the other hand EBID presents limitations when the deposition of pure metals is required, due to the lack of chemical selectivity of the decomposition process. This results in co-deposition of elements present in the precursor and/or in the deposition system.

Since 1985 the EBID of pure metals has been tried with different families of precursors, mainly metallo-organic [4], metallo-halides [7] and metallo-carbonyl [8] complexes.

The metal content of the deposits depends upon the deposition parameters and on nature of the precursor compound. Increasing the substrate temperature (up to 100°C) [4], and the deposition of noble metals in a reactive environment [9] both resulted in a higher metal content. The first approach has two drawbacks: lateral resolution loss due to substrate thermal drift during deposition and decrease of deposition rate due to lower precursor concentration at the surface. Moreover both approaches have been shown to be successful only for one precursor molecule, namely trimethyl-gold trifluoro-acetylacetonate.

High-metal content deposits have also been grown using carbon- and oxygen-free precursors, like metal-halides [7]. Nevertheless these compounds are highly toxic and difficult to handle. In addition stable volatile halides are available for only a few metals. More promising EBID precursors are the Rh- and Au-chloro-trifluorophosphine complexes, as recently shown [6,10–12]. In this paper we focus on EBID using the precursor  $[\text{RhCl}(\text{PF}_3)_2]_2$  (CAS 14876-98-3). This precursor presents physical and chemical properties, which make it a potential precursor for EBID of high metal content nano-structures. It is volatile [13,17], carbon- and oxygen-free, easy and inexpensive to synthesize, stable in air and vacuum. Electron ionization mass spectrometry of the compound shows that it decomposes by progressive loss of  $\text{PF}_3$  ligands [14]. In addition Rh is a noble metal, which does not form stable oxides, nitrides or

carbides [15] at ambient pressure and temperature. This minimizes the risk of contamination. In the first part of the paper we describe the structure and the morphology of the deposit. Then we focus on the characterization of the chemical composition of the deposits on a micrometer and nanometer scale using Auger electron spectroscopy and electron energy loss spectroscopy, respectively.

## 2. Experimental section

Our EBID apparatus has already been described elsewhere [6,10]. It is based on a modified scanning electron microscope (SEM) Cambridge S100, fitted with a W thermionic electron gun. The electron energy ( $E$ ) can be varied from 2 to 25 keV, the electron current ( $I_p$ ) from 20 nA to less than 1 pA. The deposits were grown operating the beam in scanning or spot mode. In scanning mode the beam is scanned along a TV frame in a standard scan of 625 lines with a frequency variable from 50 to 0.2 Hz. In spot mode the electron beam is stationary; its position and exposure time ( $t_e$ ) can be controlled manually or with an electron beam lithography software, Naby Nano Pattern Generation System (NPGS). The latter allows the variation of the distance between two consecutively irradiated points (point-to-point distance,  $d_p$ ) from 5 to 5000 nm and of  $t_e$  from 1  $\mu\text{s}$  to 1000 ms.

$[\text{RhCl}(\text{PF}_3)_2]_2$  was synthesized and purified by one of the authors following a procedure reported in the literature [16]; it is a red solid at room temperature, stable in high vacuum and sufficiently stable in air. Its vapor pressure is  $5.5 \times 10^{-2}$  Torr at 23°C [17]. It has been already successfully used for Rh deposition in thermal chemical vapor deposition (CVD) [18] and in scanning tunneling microscopy (STM) [19] direct writing. Thermal CVD at 200°C gave Rh deposits with a Cl contamination of a few atomic percent; STM direct writing allowed patterning of electrically conductive nano-structures. In our experiments the precursor was transported to the deposition region via a stainless steel needle (with a length of 15 mm and an inner diameter of 0.8 mm) oriented towards the point of impingement of the

Table 1

Shape and deposition parameters of the structures deposited and studied in this work.

No.	Shape	$E$ (keV)	$I_p$ (pA)	$t_e$ (s)	Mode	Substrate
1	3D rod	25	40	300	Spot	C grid
2	Line	15	8000	1	Spot	C grid
3	Dot	25	8	60	Spot	C grid
4	Square	25	2200	1800	Scanning	Si(111)
5	Dot	25	8	25	Spot	C grid

electron beam. All the deposits were grown at room temperature. As substrate materials we used 20 nm thick C (graphite) films on Cu grids for transmission electron microscopy (TEM) and electron energy loss spectroscopy (EELS) and naturally oxidized p-doped (boron) Si (111) wafers for Auger electron spectroscopy (AES).

Deposits in the form of dots (spot mode, stationary beam, short exposure time), three-dimensional rods (spot mode, stationary beam, long exposure time) and lines (spot mode, beam moving on the substrate) were deposited for TEM and EELS studies. AES was carried out on square-shaped deposits, with a side length ranging from 5 to 20  $\mu\text{m}$ , grown with the beam scanning a squared frame on the substrate. The shape and the deposition parameters of the investigated structures are listed in Table 1. Different shapes and deposition parameters were chosen to study their effect on nano-structure, nano-crystal size and composition of the deposits.

TEM, scanning transmission electron microscopy (STEM), dark field scanning transmission electron microscopy (DSTEM) and EELS were performed ex situ with the microscopes Hitachi HF 2000 (DSTEM/EELS at 200 keV electron energy), Philips EM 430ST (bright field/dark field imaging, high resolution electron microscopy), Philips CM 20, Philips CM 30. The nominal lateral resolution of the EELS systems used here is of the order of the electron probe diameter, i.e.  $1.5 \text{ nm} \pm 20\%$ . AES was performed ex situ with a PHI 660 scanning Auger microprobe (SAM) fitted with a  $\text{LaB}_6$  electron gun, equipped with an  $\text{Ar}^+$  ion sputter gun for sputter cleaning of the specimen [20].

### 3. Results and discussion

Fig. 1a shows a TEM bright field (BF) image of an EBID rod, grown on a graphite film (sample No. 1). The rod is 6  $\mu\text{m}$  high and has a diameter of about 120 nm. A high-magnification TEM BF image of the tip of the same rod is shown in Fig 1b. The tip curvature radius is about 50 nm. The image reveals the nano-composite structure of the deposits: dark granular regions about 5 nm in diameter separated by amorphous regions. The 4–5 nm thick bright shell surrounding the deposit can be identified (as indicated by the results of chemical analysis) as a C contamination layer formed following air exposure or SEM observation.

The electron diffraction pattern of the same region is shown in Fig 2. The positions of the diffraction rings are in good agreement with the literature values of lattice plane spacings of rhodium [21], represented by the black dashed circles (face centered cubic structure, with  $a = 3.803 \text{ \AA}$ ). This result proves the presence of metallic Rh crystals in the deposit. No

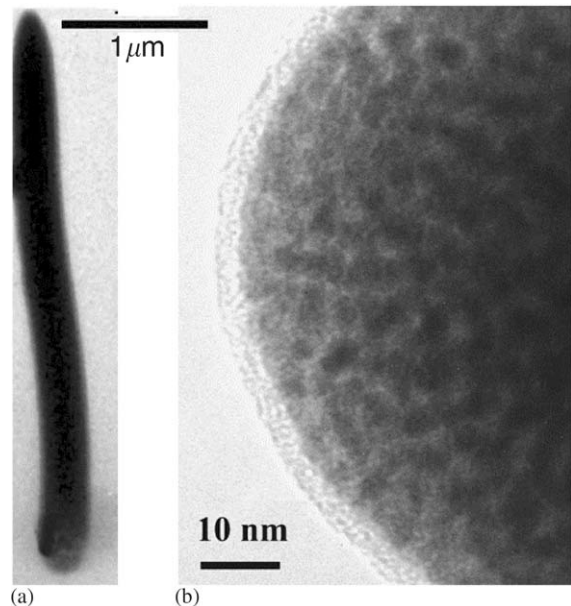


Fig. 1. (a) TEM bright field image of an EBID rod (sample No. 1). (b) High magnification image of the tip of the same rod, showing the nano-composite structure.

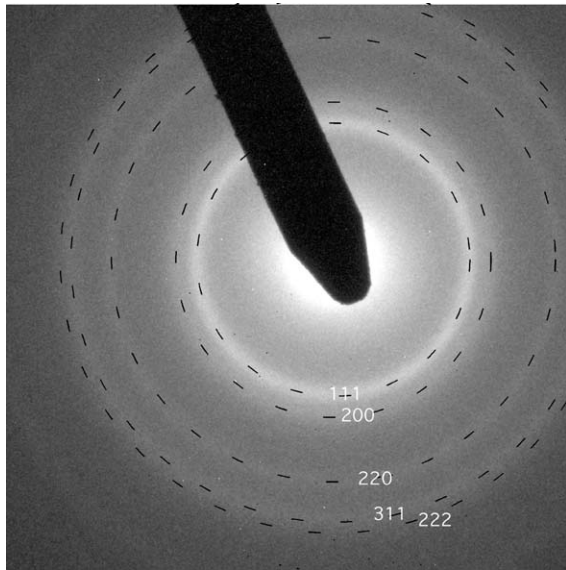


Fig. 2. Electron diffraction pattern of the same region shown in Fig. 1 revealing the crystalline structure. The black dashed circles indicate the lattice plane spacings of Rh.

crystallographic ordering between the Rh grains can be observed in the diffraction pattern.

High resolution electron microscopy (HREM) imaging (Fig. 3) of a line deposited on a graphite film (sample No. 2) gives further insight into the structure of the deposit. The image shows that, as in Fig. 1b, dark granular crystallites with a size of 4–6 nm, are immersed in an amorphous matrix. Lattice planes of crystallites are visible in the image. Fourier transform shows that these grains have the symmetry and lattice plane spacings of crystalline Rh. This confirms that the dark regions of the HREM image correspond to crystalline Rh grains. No grain boundaries are visible. It is not clear whether the 5 nm crystallites are mono-crystalline or poly-crystalline.

High resolution STEM images of an EBID dot (sample No. 3) are reported in Fig. 4. The images were acquired with different contrasts, in order to visualize independently both zones of the deposit in the center (a) and at the border (b), respectively. The image contrast is mainly ( $Z$ )-contrast ( $Z$  being the atomic number), since it is obtained from electrons being scattered by angles larger than 40 mrad. This means that the image intensity is proportional to  $Z^2$ , with the unscreened nuclei

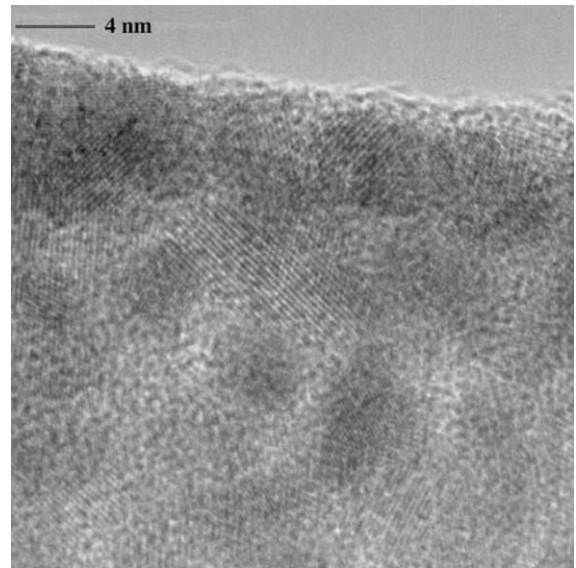


Fig. 3. HREM image of a region of an EBID line (sample No. 2), showing lattice planes of nano-crystals of 4–6 nm in diameter.

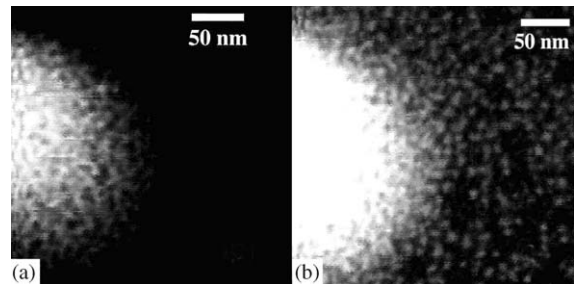


Fig. 4. DSTEM image of an EBID dot (sample No. 3) acquired with different contrast.

approximation. The Rh nano-grains (bright) can be clearly distinguished from the amorphous material between them (dark). The intensity of single Rh grains of similar size changes by  $\pm 20\%$  from one grain to another. On the other hand, the intensity of the amorphous region in the deposit is a factor of 3–4 lower than that of the Rh grains. This indicates that the amorphous regions contain low- $Z$  material (i.e. P, N, O, C).

Fig. 4b shows that Rh nano-crystals, with an average size of about 5 nm, are also present on the substrate outside the dot area. These crystals may have been deposited by scattered electrons or during SEM imaging in scanning mode in the

deposition system, in the presence of precursor vapor. The result proves that Rh nano-crystals of comparable size are present even in deposits obtained at low electron beam currents and short exposure times. The evolution of the grain size was probed as a function of exposure time, i.e. deposit thickness, using electron diffraction and STEM imaging. Figs. 1b, 3 and 4 show evidence for the invariance of Rh grain size with deposit thickness: in both thin and thick regions the Rh grain size remains constant and the diffraction patterns have similar line widths. Furthermore, the grains form a network in regions of thicker deposits. Assuming a spherical shape, the 5 nm grains contain about 12000 Rh atoms (density of Rh =  $12,3 \text{ g cm}^{-3}$ ), which correspond approximately to a 12/13-shell cluster (assuming that the total number  $y$  of Rh atoms per  $n$ th shell is given by:  $y = 10/3n^3 - 5n^2 + 11/3n - 1$  [22]). The 5 nm diameter of the Rh grains possibly results from the fact that such clusters are the most efficient in catalyzing the decomposition of the intermediate amorphous layers. Therefore almost the same grain size is obtained independently of the experimental conditions.

A typical Auger spectrum of an EBID deposit obtained from  $[\text{RhCl}(\text{PF}_3)_2]_2$  is shown in Fig. 5. The analyzed sample is square-shaped with  $12 \mu\text{m}$  side length (sample No. 4). The dashed and solid curves indicate the spectrum of the as received and the sputter cleaned ( $2 \text{ keV Ar}^+$ , 120 s) sample, respectively. The spectra reveal the presence of the elements Rh, P, Cl, N and O; no F was detected even though this element is present in high concentration in the precursor molecule. The characteristic peaks of the elements in the deposit are indicated in the plot: Rh MNN triplet (peaks at 219 eV, 250 eV and 297 eV), Rh LMM (40 eV), P LMM (115 eV), Cl (180 eV), N (375 eV) and O (507 eV) KLL. Comparison of the spectra before and after sputter cleaning reveals that the main effect of sputtering is an increase in Rh and a decrease in O concentration. The typical chemical composition of deposits grown from  $[\text{RhCl}(\text{PF}_3)_2]_2$ , measured by AES, averaged over 12 samples, is:  $60 \pm 0.6 \text{ at\% Rh}$ ,  $20 \pm 2 \text{ at\% P}$ ,  $5 \pm 0.8 \text{ at\% Cl}$ ,  $7 \pm 1 \text{ at\% O}$ , and  $7 \pm 1 \text{ at\% N}$ . AES surface mapping and depth profiling showed that

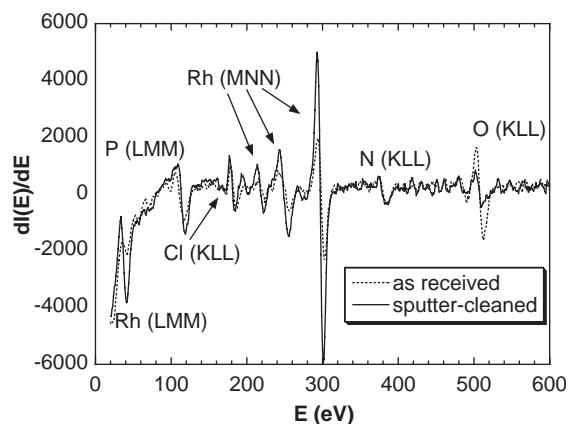


Fig. 5. AES spectrum of an EBID square (sample No. 4) before (dashed) and after (solid) sputter cleaning. The characteristic peaks are at 40, 219, 250 and 297 eV for Rh, at 180 eV for Cl, at 115 eV for P, at 375 eV for N, and at 507 eV for O, as indicated in the figure.

the deposit composition is homogeneous, within the AES spatial resolution limit, at the surface and in the bulk. Similar compositions have been obtained on tens of deposits, grown at 2 keV, 5 keV and 25 keV electron energy, with the electron current ranging from 1 nA to 10 nA [23]. This indicates that the composition is not affected by the deposition conditions, i.e. electron current, electron energy, and exposure time, within the range explored in this work.

In order to perform chemical analysis with higher spatial resolution and to avoid damage induced by ion sputter cleaning, we performed EELS. A typical EELS spectrum of an Rh-containing line (sample No. 2), deposited on a 20 nm C grid, is shown in Fig. 6. The background signal has been subtracted before the C edge for a better visualization of elemental edges. The spectrum reveals the presence of the elements Rh, C, N and O. The Rh (M), C (K), N (K), and O (K) edges are indicated by vertical lines above the spectrum.

In order to study the carbon distribution in the deposit, we measured the evolution of the Rh/C atomic concentration ratio as a function of the deposit thickness. The Rh/C ratio can be obtained from the edge intensities and the corresponding cross sections. Since the Rh–K edge is not well known, its cross section was determined from a

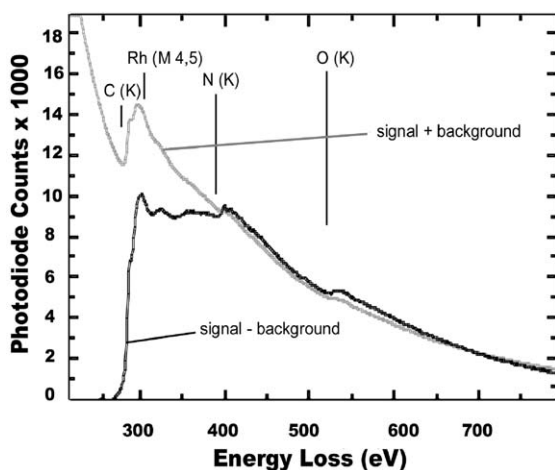


Fig. 6. EELS spectrum of sample No. 2 before (gray), and after (black) background subtraction.

$\text{Rh}_2\text{O}_3$  standard. To measure the evolution of the atomic concentration ratios, EELS spectra were taken, with a convergent electron beam, at six different points starting from the edge and moving towards the center of the line section, as shown schematically in the inset of Fig. 7. The TEM sample holder was cooled down to liquid nitrogen temperature in order to prevent C contamination. The thickness increases on moving from the edge to the centre of the line. The deposit thickness is expressed here in multiples of the mean free path (MFP) of plasmon scattering. For the Rh deposit, assuming a density of  $8.5 \text{ g cm}^{-3}$ , 1 MFP is around 120 nm [24]. The evolution of the concentration ratios  $R(i)$  (where  $i = \text{C}, \text{O}$  or  $\text{N}$ ) relative to Rh are defined as

$$R(i) = \frac{c(i)}{c(i) + c(\text{Rh})}, \quad (1)$$

where  $c(i)$  are the atomic concentrations of the elements. A plot of  $R(\text{C})$ ,  $R(\text{N})$ , and  $R(\text{O})$  versus deposit thickness (in MFP) is shown in Fig. 7. On moving from the thin to the thick region,  $R(\text{O})$  and  $R(\text{N})$  remain constant along the line profile, after an initial decrease, while  $R(\text{C})$  decreases continuously. When the presence of one element is limited to the specimen surface its concentration decreases with increasing analyzed thickness. Therefore, the measurement proves that C is localized at the specimen surface, whereas O and N are homo-

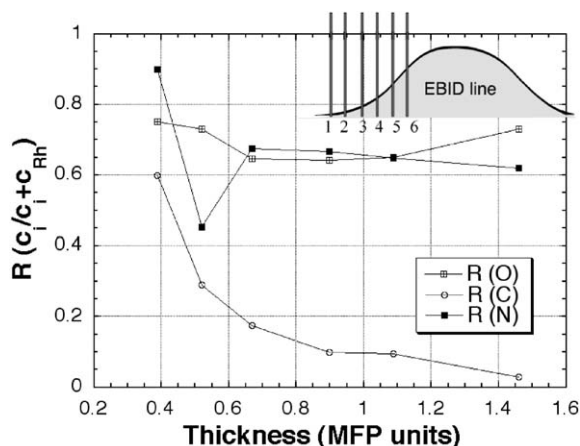


Fig. 7. Evaluation of the  $R(\text{O})$ ,  $R(\text{C})$  and  $R(\text{N})$  ratios for sample No. 2 as defined in Eq. (1). Inset: schematics of the points of EELS analysis along the section of an EBID line.

geneously distributed throughout the entire specimen. This result is consistent with the AES measurements and is a confirmation that the presence of C in EBID structures grown from  $[\text{RhCl}(\text{PF}_3)_2]_2$  is confined to the contamination layer.

The EELS measurements discussed above give information on the chemical composition of the deposit averaged over different regions of the EBID line section. In order to obtain information at the nano-scale, EELS chemical mapping was performed on deposits with lateral dimensions of about 100 nm. Fig. 8a shows a DSTEM image of a Rh dot (sample No. 5). The electron beam was scanned in the rectangular region in Fig. 8a and at each scan point one EELS spectrum was acquired. From the subsequent extraction of the Rh and P edge intensities, the edge intensity maps in Fig. 8b and c were obtained. These maps were acquired on the Rh–L edge and the P–K edge at higher energy losses since the latter are less sensitive to thickness fluctuations or edge overlaps than those at lower energy. The images prove that Rh and P are present in the deposit and in the more diffuse surrounding region. This result confirms that Rh and P are present also in deposits obtained at very low current and short exposure times. Furthermore, an increase of the overall Rh intensity is correlated with an increase in the P intensity. To determine the composition at the grain size scale,

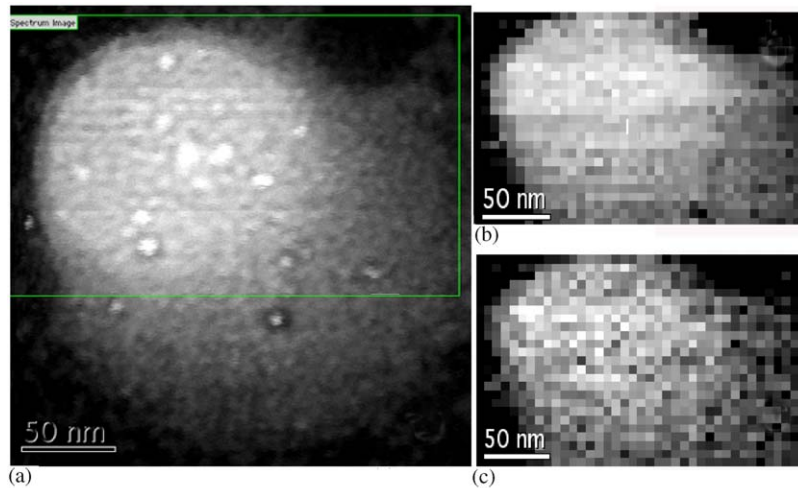


Fig. 8. DSTEM image of sample No. 5 (a), Rh (b) and P (c) edge intensity maps acquired in the region delimited by the rectangle, over the intervals 3004–3146 eV (Rh, L) and 2196–2296 eV (P, K), respectively.

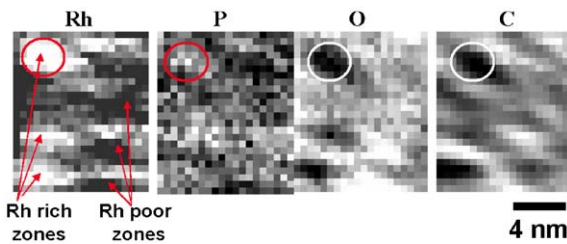


Fig. 9. High-resolution EELS edge intensity maps in a region of sample No. 5 at: 324–340 eV (Rh, M), 540–549 eV (O, K) and 2196–2292 eV (P, K).

edge intensity maps for Rh (M), P (K), O (K) and C (K) edges with nanometer resolution were acquired. The spectrum images are shown in Fig. 9. These reveal that areas rich in Rh (indicated by the arrows in the figure) clearly correlate with areas poor in O and C. Taking into account the previous observations, we can conclude that O and C are found mainly in the gaps between Rh nano-crystallites in the bulk and at the surface, respectively. The high C signal in Fig. 9 is explained by the low specimen thickness. The P spectrum image is less clear but indicates that the element is distributed throughout the whole deposit with a higher concentration in areas rich in Rh.

#### 4. Discussion

The material deposited from  $[\text{RhCl}(\text{PF}_3)_2]$  is not pure rhodium. It consists of a nano-composite containing Rh nano-crystals immersed in a lighter amorphous matrix containing the elements P, O, N and Cl. The size of the Rh nano-crystals ranges from 3 to 6 nm and is independent of the deposition conditions and the beam parameters within the range investigated. The chemical composition of the deposits is typically 60 at% Rh, 20 at% P and the remaining 20 at% is constituted by O, N and Cl, present in concentrations ranging from 3 at% to 10 at%. A carbon contamination layer is present at the deposit surface but no carbon could be detected in the deposit bulk.

High resolution EELS showed that the elements Rh and P are locally correlated. This does not mean that P is present in the Rh grains since the Rh interstitials can accommodate small percentages of P but not the 15–20 at% found in the deposit. In addition the presence of rhodium phosphides is excluded since the diffraction patterns indicate that Rh is present in the metallic form. Therefore P should be present inside the amorphous zone in the close surroundings of the Rh grains. P is detected also for deposits on C

substrates. This excludes that the element is generated by a chemical reaction between  $\text{PF}_3$  and the Si surface. The elements O and N are present in the amorphous region, which could consist of an insulating polymer containing O, N and some amount of P and Rh. The presence of the elements P and Cl is explained by partial decomposition of the precursor molecule. The large amount of phosphorous detected shows that the decomposition of  $[\text{RhCl}(\text{PF}_3)_2]_2$  in EBID conditions does not follow the pathway observed in thermal decomposition. The presence of the elements N and O, which are not contained in the precursor and should not be present in high concentration in the vacuum system, is probably explained by air uptake when the deposits are exposed to air. Despite its high concentration in the precursor, fluorine is not present in the deposits. This can be due to the formation of gaseous stable molecules, i.e.  $\text{F}_2$  and/or  $\text{PF}_3$ , which are pumped away during the deposition process.

## 5. Conclusions

The presented results reveal that EBID of high Rh content nano-structures such as tips, rods and lines, can be successfully carried out using the precursor  $[\text{RhCl}(\text{PF}_3)_2]_2$ . The morphology, the structure, and the chemical composition at the micro- and nano-scale of these structures have been investigated for the first time. The deposited material is nano-composite with 4–6 nm sized Rh nano-crystals immersed in an amorphous matrix, with an average chemical composition of  $60 \pm 0.6 \text{ at\% Rh}$ ,  $20 \pm 2 \text{ at\% P}$ ,  $5 \pm 0.8 \text{ at\% Cl}$ ,  $7 \pm 1 \text{ at\% O}$  and  $7 \pm 1 \text{ at\% N}$ .

## Acknowledgements

This work was partially financed by the Swiss National Science Fund of Research (SNF No. 21-64064.00) and by CTI-TN 5441-2. We thank

Professor Hans Joerg Mathieu (EPFL/STI-SMX) for AES analysis.

## References

- [1] C. Schössler, J. Urban, H.W.P. Koops, *J. Vac. Sci. Technol. B* 15 (1997) 1535.
- [2] H.W.P. Koops, *Proc. SPIE* 2849 (1996) 248.
- [3] M. Weber, M. Rudolph, J. Kretz, H. W. P. Koops, *J. Vac. Sci. Technol. B* 13 (1995) 279.
- [4] H.W.P. Koops, C. Schlosser, A. Kaya, M. Weber, *J. Vac. Sci. Technol. B* 14 (1996) 4105.
- [5] P.C. Hoyle, J.R.A. Cleaver, H. Ahmed, *J. Vac. Sci. Technol. B* 14 (1996) 662.
- [6] I. Utke, B. Dwir, K. Leifer, F. Cicoira, P. Doppelt, P. Hoffmann, E. Kapon, *Microelectron. Eng.* 53 (2000) 261.
- [7] S. Matsui, K. Mori, *J. Vac. Sci. Technol. B* 4 (1985) 299.
- [8] H.W.P. Koops, R. Weiel, D.P. Kern, T. H. Baum; *J. Vac. Sci. Technol. B* 4 (1988) 477.
- [9] A. Folch, J. Tejada, C.H. Peters, M. S. Wrighton; *Appl. Phys. Lett.* 66 (1995) 2080.
- [10] I. Utke, B. Dwir, K. Leifer, P. Hoffmann, E. Kapon, P. Doppelt; *J. Vac. Sci. Technol. B* 18 (2000) 3168.
- [11] P. Doppelt, R. Even, F. Marchi, V. Bouchiat, H. Dallaporta, S. Safarof, R. Tonneau, P. Hoffmann, F. Cicoira, I. Utke, B. Dwir, K. Leifer, E. Kapon, *E.C.S. Symp. Proc.* (2000) 112.
- [12] P. Hoffmann, I. Utke, F. Cicoira, B. Dwir, K. Leifer, E. Kapon, P. Doppelt, *M. R. S. Symp. Proc.* 624 (2000) 171.
- [13] P. Doppelt, V. Weigel, P. Guinot, *Mater. Sci. and Engineer. B* 17 (1993) 143.
- [14] P. Seuret, F. Cicoira, T. Ohta, P. Hoffmann, J. Weber, T. Wesolowski, *Phys. Chem. Chem. Phys.* 5 (2003) 268.
- [15] P. Pascal, *Nouveau Traité de Chimie Minerale*, Vol. XIX, Masson, Paris, 1958.
- [16] M.A. Bennet, J. Patmore, *Inorg. Chem.* 10 (1971) 2387.
- [17] T. Ohta, F. Cicoira, P. Doppelt, L. Beitone, P. Hoffmann, *Adv. Mater.* 13 (2001) 33.
- [18] P. Doppelt, L. Ricard, V. Weigel, *Inorg. Chem.* 32 (1993) 1039.
- [19] F. Marchi, D. Tonneau, H. Dallaporta, V. Safarof, V. Bouchiat, P. Doppelt, R. Even, L. Beitone, *J. Vac. Sci. Technol. B* 18 (2000) 1171.
- [20] Perkin Elmer, 660 AES Operator's Reference Manual, 1988.
- [21] International Center for Diffraction Data, PDF file 05-0685.
- [22] T.P. Martin, *Phys. Rep.* 273 (1996) 199.
- [23] F. Cicoira, Ph.D. Thesis No. 2528, 2002, EPFL.
- [24] R.F. Egerton, *Electron Energy Loss Spectroscopy in the Electron Microscopy*, Plenum Press, New York, 1996.